Synthesis and characterization of SBA-15 silica containing cyclam inside pores for capturing iron chloride: analysis of interactions between ferrous chloride and cyclam in a system with strongly dispersed functional groups on the SiO_2 surface

Łukasz Laskowski[a], Magdalena Laskowska*[a], Alain Walcarius[b], Marek Doskocz[a], Neus Vila[b], Agnieszka Karczmarska[a], Piotr Pawlik[c], Jerzy Goraus[d], Katarzyna Balin[d], Mateusz Dulski[e]

[a] *Institute of Nuclear Physics Polish Academy of Sciences, Krakow, 31-342, Poland*
[b] *Université de Lorraine, CNRS, LCPME, Nancy, F-54000, France*
[c] *Faculty of Production Engineering and Materials Technology, Czestochowa University of Technology, Al. Armii Krajowej 19, Czestochowa, 42-200, Poland*
[d] *A. Chełkowski Institute of Physics, University of Silesia, 75 Pułku Piechoty 1a, Chorzów, 41-500, Poland*
[e] *Institute of Materials Engineering, University of Silesia , 75 Pułku Piechoty 1a, Chorzów, 41-500, Poland*

Abstract

The use of the spatial structure of mesoporous silica combined with organic molecules opens up a wide range of possibilities in the field of separation of single atoms and the precise creation of their environment. Materials obtained in this way can find applications as single-atom catalysts (SAC) and in environmental applications in ion and molecule trapping processes. An example of such a material is silica of the SBA-15 type functionalized with cyclam (1,4,8,11-tetraazacyclotetradecane) anchored inside the pores with propyl chains. In this work, we present such a material containing 5% functional groups, additionally activated with iron(II) chloride, which was chelated by cyclam anchored inside the pores of silica. The presented nanocomposite has been thoroughly tested for its assumed molecular structure and stability. We compared it to a material containing only cyclam. The obtained results showed the high efficiency of the silica matrix with cyclam in the separation of single $FeCl_2$ molecules and the correct molecular structure of the obtained material. The nanocomposite containing chelated

molecules with iron showed good stability, while the structure of the material with cyclam alone collapsed with time.

Keywords: Mesoporous silica, SBA-15, cyclam, functional materials

1. Introduction

The modern approach to environmental protection involves not only the disposal of waste but, above all, the reduction of the nuisance of production. One way is to use selective and efficient catalysts. Some catalysts are metals finely dispersed on a support with a large surface area for efficient use of catalytically active components. The size of the metal particles is one of the most important factors that affect the performance of the catalyst [1]. Studies show that sub-nanometer clusters can have better catalytic activity and/or selectivity than nanometer-sized particles [2, 3]. In contrast, single atoms with a low degree of coordination often function as active sites. By designing a material consisting of single atoms: Single Atom Catalyst (SAC), new possibilities open up for creating truly efficient or selective catalysts. In addition, a well-designed system can utilize 100% of a metal atom's surface as a catalytic surface. This is important for expensive elements or fast-wearing catalysts. A key part of the design process is to know and understand the structure of the surrounding metal atom. This is a difficult task because SAC catalysts often undergo various undesirable reactions due to their reactivity.

To achieve metal separation, as described above, the metal atom anchors on a support, which forms a spatial framework, and also sometimes participates in catalytic reactions due to the formation of a suitably molecular environment. In addition, due to the spatial structure of such a material, it has an unfolded surface. Such a skeleton can be made of metal oxides, metals, carbonaceous materials, silicate materials, zeolites, organometallic structures, and ordered mesoporous materials [4]. One of the first materials used to refer to SAC, even before the acronym was defined in 2011 [5], was mesoporous silica [6]. Such a framework makes it possible to design and synthesize a material with a specific surface structure, pores, or more complex systems, such as porous spheres [7] or nanostructured thin films [8, 9]. For the research presented in this publication, we chose silica SBA-15 which is characterized by the ability to form well-defined spatial systems [10].

Having selected a suitable matrix and a catalytically active metal atom, the key activity is to choose how to anchor it in the matrix. For this purpose,

strongly chelating molecules such as cyclam can be used.

Cyclams are 14-membered tetraamine macrocycles that bind strongly to a wide range of metal ions [11]. Unfortunately, metal-cyclam complexes are susceptible to oxidative degradation, which is initiated by deprotonation of the secondary amine [12]. Cyclam derivatives, no less, are used in various catalysts. The combination of silica and cyclam are interesting materials that have properties as heavy metal adsorbents [13], oxidation catalysts [14], or magnetic materials [15]. Moreover, the presence of a silica matrix prevents the degradation of metal-cyclam complexes, as we will demonstrate in this work.

The chelating properties of cyclam can be used in processes for the removal of heavy metals from the environment, in catalysts in oxidizing waste, or in improving the efficiency of chemical reactions, especially green synthesis [16] including compounds that are the fuels of the future, such as ammonia [17] or methanol [18]. However, this first application is the most interesting for our team. Cyclam-based chelating compounds seem to have great application potential in the uptake of metal chlorides from water or soils. However, their effectiveness and stability should be tested before their application.

The research material analyzed in this paper is SBA-15 mesoporous silica containing cyclam anchored inside the pores through propyl chains, chelating iron ions. The concentration of cyclam-iron groups was 5% molar, that is, the molar ratio of Fe/Si = 0.05. Figure 1 shows an overview diagram of the material. Within the framework of the present work, we intend to verify that the material we have designed meets the basic conditions to be considered useful in applications such as single-atom catalysts and heavy metal adsorbent. To do this, we successfully synthesized this composite metal-cyclam-silica nanomaterial and thoroughly investigated its structure and properties. If the proposed nanocomposite had the assumed molecular structure and properties, this would make it useful in environmental applications as a metal adsorber, including in the form of chlorides. Moreover, if the proposed material is able to hold the separated metal-containing groups, the nanocomposite could be considered as a potentially useful SAC in catalysis. Of course, this will require further research in this direction, but maintaining a certain distribution of functional groups is a sine qua non here.

Moreover, we investigated the stability of the material containing iron chloride molecules chelated with cyclam with respect to the material containing only cyclam inside the silica pores.

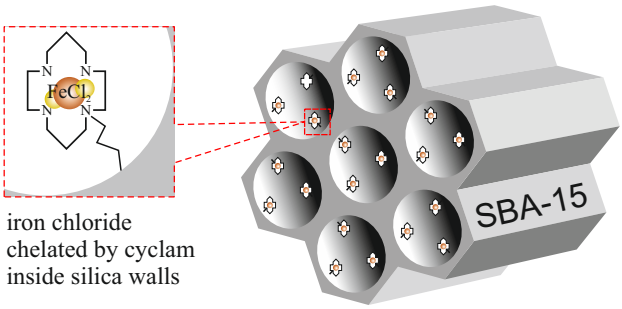

Figure 1: The overview diagram of the material investigated: SBA-15 silica containing iron chloride molecules chelated by cyclam inside silica channels

2. Materials and methods

2.1. Material's synthesis

The SBA-15 mesoporous silica containing cyclam groups inside pores can be used for capturing two-valence metal chlorides. In this case, iron chloride was immobilized by cyclam inside silica pores, creating composite material.

The specimen can be prepared via co-condensation in the presence of P123 non-ionic surfactant (poly(ethylene glycol)$_{20}$-poly(propylene glycol)$_{70}$-poly(ethylene glycol)$_{20}$ – Sigma-Aldrich Chemie GmbH, Germany). Here, we present the synthesis route of the material containing 5% of cyclam units (molar concentration with regards to silica groups). The three-step procedure is shown in Fig. 2.

First, the surfactant solution was prepared: 8g of P123 was dissolved in 320ml of aqueous solution of HCl (pH=1.5). After the complete dissolution of the surfactant (after approximately five hours), we added weighted amounts of the precursors: 17.78g of tetraetyl orthosilicate (Sigma-Aldrich Chemie GmbH, Germany), hereafter called TEOS and 0.89g of chloropropyl trimethoxysilane (ClPTMS, Sigma-Aldrich Chemie GmbH, Germany) as a precursor for cyclam. The molar ratio between TEOS and ClPTMS was 19:1. This mixture was vigorously stirred at room temperature till a clear solution was obtained (after approximately three hours). Next, 0.151g of NaF was added to induce hydrolysis and polycondensation, and the material was immediately heated to 60 °C in a hot oil bath and stirred vigorously for 48 hours. The resulting material was filtered and placed in a Soxhlet apparatus in order to remove the surfactant by hot ethanol. The obtained powder was

dried in a vacuum at 120 °C for 24 h. After this step, a part of the powder (SBA-15 silica containing chloropropyl units inside the pores) was left as a reference for spectroscopic measurements (sample named **SBA-Cl**).

In the second step, the chlorine atoms in chlopropyl groups are substituted by cyclam. This is realized by mixing the pre-functionalized silica powder with cyclam dissolved in acetonitrile (MeCN) and triethylamine (TEA). Per one gram of pre-functionalized silica, we added 45cm^3 of MeCN, 1cm^3 of TEA, and 0.2g of cyclam (slightly more than necessary 0.79mmol). The product was heated under reflux and stirred for 48h. The white solid can be recovered by filtration and washing five times with hot chloroform and three times with hot ethanol to remove the excess cyclam. After drying at 120 °C overnight in a vacuum, the material containing cyclam inside pores is ready. At this stage, we preserved a small amount of the material as a reference (sample named **SBA-Cy**).

In order to functionalize the sample with iron chloride, we added 0.12g $FeCl_2$ to each gram of SBA-Cy powder (slightly more than the necessary 0.7mmoles) and placed the mixture under a reflux condenser overnight with dry ethanol (about 50ml for each gram). The resulting solid (**SBA-Cy-$FeCl_2$**) was recovered quantitatively by filtration and washed several times with ethanol to remove excess iron salts. After filtration and drying, the final material was ready.

Just after synthesis, a portion of the samples containing cyclam (SBA-Cy-$FeCl_2$ and SBA-Cy) were aged for 30 days to be able to investigate their structural stability. To do this, we kept samples in a laboratory maturing cabinet at 20°C and 55% humidity for 30 days.

Additionally, we also prepared the reference material for spectroscopic measurements: $FeCl_2$ chelated by cyclam (hereafter called **Cy-$FeCl_2$**). For this purpose, we dissolved 15 mmoles of cyclam (3g) and 15 mmoles of Cy-$FeCl_2$ (1.90g) in 100ml of dry ethanol. We left the resulting solution under reflux overnight. The yellow solution was evaporated, and the resulting powder was dissolved in 40ml of methanol and 80ml of acetone. After cooling to -20°C for three hours, the yellow powder was filtered and washed with acetone.

2.2. Experimental details

The morphology of samples was characterized using a scanning electron microscope (SEM) Tescan Vega 3 (Tescan, Brno, Czech Republic) operated at 30kV using the SE detector. The observation of pores structure was

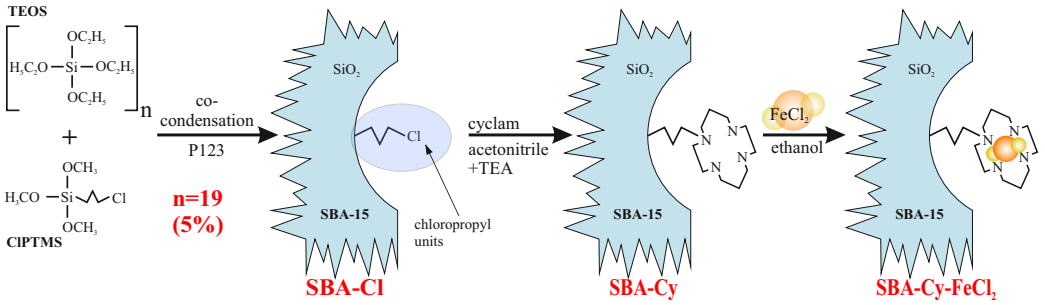

Figure 2: The schematic presentation of the synthesis route of the investigated material: SBA-15 silica containing iron chloride molecules chelated by cyclam inside silica channels. Designations: TEOS — tetraethyl orthosilicate, ClPTMS — chloropropyl trimethoxysilane.

performed by transmission electron performed microscope (TEM) FEI Tecnai G2 20 X-TWIN (FEI Company, Hillsboro, OR, USA) operated at 200kV.

To study the ratio between the elements, the Energy Dispersive X-ray microanalysis was provided by SEM coupled to an energy-dispersive X-ray spectrometer(QUANTAX EDS, Bruker), equipped with XFlash 610 M detector with the resolution of ¡129 eV for the Mn K line.

To determine the amount of nitrogen and carbon in the samples, elemental analysis was performed using a vario EL II elemental analyzer operating in CHNS mode. Measurements were repeated twice, using weights of about 4.5 mg.

More detailed microscopic observation was possible thanks to the use of a transmission electron microscope (TEM). For this purpose, we used JEOL JEM-3010 high-resolution transmission electron microscope (TEM, JEOL Ltd., Tokyo, Japan) with 300 kV acceleration voltage, equipped with a LaB_6 emission source and Gatan 2k×2k Orius^{TM} 833 SC200D CCD camera (Gatan Inc., Pleasanton, CA, USA).

The small-angle XRD patterns were measured using Bruker D8 Advance diffractometer operating at 40 kV and 40 mA. The diffractometer was equipped with the copper tube (CuKα radiation; $\lambda = 1.5418$ Å) and the LynxEye silicon strip detector. The XRD studies on a pure Mn_{12}-stearate were performed with the use of Göbel Mirrors to create a parallel beam. Furthermore, 0.1 mm primary divergent slit, as well as Soller slits on diffracted beam, were used. In this experiment, the measurements were performed in the 0D mode of the LynxEye detector and the range of 2Θ angles from 0.2 to 5 deg with

a step size of 0.01 deg and measurement step time of 20 s.

The specific surface area was determined using isothermal sorption of nitrogen. Adsorption-desorption isotherms were recorded at 77.4 K using an Autosorb iQ (Quantachrome Instruments, Boynton Beach, FL, USA) analyzer. The calculations of BET surface area, pore volume, and pore size distribution were performed with ASIQWin software. The specific surface areas were calculated according to Brunauer- Emmett-Teller (BET) method from the adsorption data in the relative pressure range determined by Rouquerel's criteria [19]. This means that seven points were taken into account in calculating the specific area in each case. The selection of the seven points was made possible by dense measurements of relative pressure p/p_0, which was changed in 0.01 increments.

Raman spectra of samples were gathered through WITec confocal Raman microscope CRM alpha 300 R (WITec Wissenschaftliche Instrumente und Technologie GmbH, Ulm, Germany) equipped with an air-cooled solid-state laser (λ = 532nm, P=20mW). The excitation laser radiation was coupled into a microscope through a polarization-maintaining single-mode optical fiber with a 50 μm diameter, and the monochromatic light was focused on the sample by an air Olympus MPlan (100×0.90NA) objective. Raman scattered light was passed through a multi-mode fiber (50μm diameter) into a monochromator with a 600 line/mm grating and a CCD camera. The spectrometer monochromator was checked before the measurements using a silicon plate (520.7cm^{-1}). Raman spectra in the 150–4000cm^{-1} were accumulated by 60 scans with an integration time of 10 s and a resolution of 3cm^{-1}, while the post-processing analysis, such as baseline correction or cosmic ray removal done in the WITecProjectFive Plus (version 5.1.1, WITec Wissenschaftliche Instrumente und Technologie GmbH, Ulm, Germany). Finally, the peak fitting analysis of RS data was performed using GRAMS (version 9.2, Thermo Fisher Scientific, Waltham, MA, USA) software.

The chemical analysis of the iron-containing sample was conducted using a Time-of-Flight Secondary Ion Mass Spectrometry (ToF-SIMS) investigation, with the use of TOF-SIMS 5 spectrometer (ION-TOF GmbH in Munster, Germany), a reflection-type spectrometer equipped with a bismuth liquid metal ion gun. Measurements were performed in both positive and negative polarity modes. High-resolution mass spectra were obtained using a Bi^{3+} primary beam (0.3pA and 30kV). The spectra were collected by rastering the ion beam across a 500 μm×500µm area, with a resolution of 256×256 points. The low-energy flood gun was utilized to compensate

for surface charging. Analysis was carried out using SurfaceLab6 software (IONTOF GmbH, Munster, Germany) and PySPM[20]. Positive spectra were calibrated to characteristic hydrocarbon fragments, such as H^+, CH_3^+, $C_2H_3^+$, $C_3H_3^+$, and $C_3H_5^+$, while negative spectra were calibrated to H^-, C^-, CH^-, CH_2^-, CH_3^-, C_2^-, C_3^-, and C_4^-. The mass resolution ($m/\Delta m$) was approximately 5600 for positive spectra and 4400 for negative spectra (determined at ^{30}Si m/z).

To improve the interpretation of the experimental data, we prepared a molecular model of SBA-15 mesoporous silica containing iron(II) chloride chelated by cyclam anchored inside a channel via a propyl chain. Geometry optimization calculations of model molecules were carried out with Gaussian G16 Revision C.01 program package[21] using the Becke's three-parameter (B3) hybrid functional [22] with Lee–Yang–Parr(LYP)[23] correlation functional [24] with the Grimme's dispersion and the Beck-Johnson damping parameter with standard G-31G(d) basis set [25]. We build and optimized the model similarly, as in our earlier works [26, 10, 27].

The magnetic properties of iron-containing samples were measured using a Quantum Design Physical Properties Measurement System (QD-PPMS) and Vibrating Sample Magnetometer (VSM) option in a wide temperature range from 300K to 3K.

3. Experimental results

First, we conducted a microscopic observation of the microstructure of the samples under an SEM microscope (detailed SEM images with stability analysis can be found in Section 4). During this study, we also analyzed the elemental composition.

The material containing ferric chloride (SBA-Cy-$FeCl_2$) was examined for chemical composition using EDS elemental analysis during SEM observations. Since our goal was to determine the exact iron content with respect to silica (which was assumed to be 5% relative to the SiO_2 groups), we did not test the sample containing sole cyclam (since such a sample without iron as a reference point, would not bring any informative results). The results of elemental analysis, together with a linear scan, can be seen in Figure 3. The EDS spectrum (Figure 3 left side) clearly shows the atomic content of iron of 5% relative to the SiO_2 groups, thus exactly according to the synthesis assumption. What's more, the linear EDS scan (Figure 3 right side) shows the presence of iron only where silicon is found (and thus where the sample

is). In addition, the ratio of iron to silicon remains constant, as seen in the line scan. Therefore, it can be concluded that we are not dealing here with any contamination of the sample with iron salts or crystallites but with its homogeneous distribution in the volume of the material.

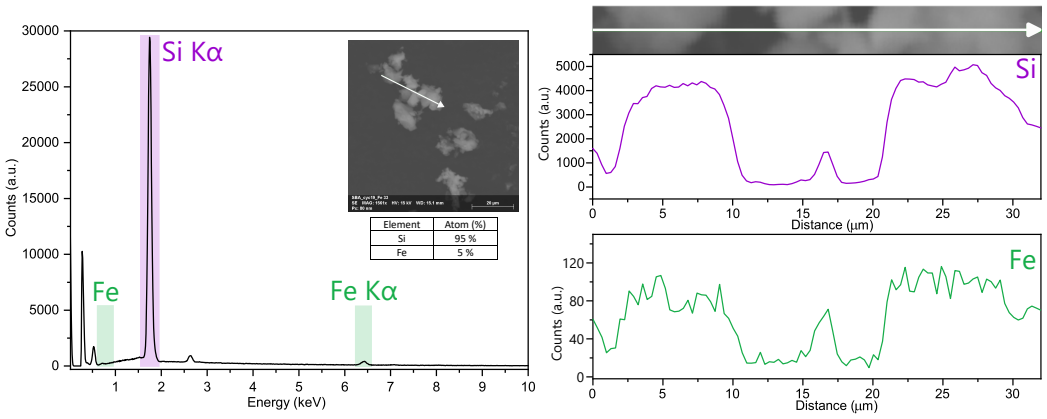

Figure 3: Elemental analysis EDS of the SBA-Cy-$FeCl_2$ sample (left) together with a linear EDS scan, showing the presence of iron only in the sample.

EDS analysis of the content of individual elements throughout the area showed molar ratios of elements as follows. The ratio of iron to silicon, as with the line scan, was about 1:20 (Fe: 4.9%, Si: 95.1%), so very close to the assumed ratio. The iron to nitrogen ratio was similarly close to the intended ratio. We almost got the expected 1 mole of iron per 4 mole of nitrogen (Fe: 19.3%, N: 80.7%). The key to understanding the complexation of iron was the ratio of iron to chlorine. We obtained the values of Fe: 34.5 and Cl: 65.5, which give similar ratios to the assumptions of one mole of iron for two moles of chlorine.

Due to the fact that EDS analysis performed in the SEM microscope chamber does not give reliable results of carbon content due to the carbon tape used to attach the sample, we performed additional CHN analysis, obtaining information not only about the mass content of carbon in the sample, but also about the nitrogen content, and their mutual proportions. Analyzing the atomic composition of our material and the masses of the individual elements, the expected nitrogen content of the total mass of the sample is 3.59% (since we have four nitrogen atoms in the cyclam), and the carbon content is 10.01% (since we have 10 carbon atoms in the cyclam and three

in the propyl chain). Elemental analysis of CHN showed 3.12% nitrogen and 9.84% carbon in the sample, so we got values close to the assumed ones. The elemental composition analysis seems to confirm the correctness of the chemical composition of the samples obtained.

Observations with a transmission electron microscope provided detailed information on the structure of the samples. A first look at the TEM images alone reveals differences between the SBA-Cy and SBA-Cy-$FeCl_2$ materials. Looking at the top photo of the iron-containing material, one can clearly see the correct, sharply defined structure of the SBA-15 silica, along with its characteristic channels, ordered 2D hexagonal [28, 29].

In contrast to the iron-containing material, the SBA-Cy sample (bottom photo) shows a material with a much less well-defined structure. Closer inspection of the TEM images reveals a certain degree of degradation of the 2D hexagonal structure, typical of SBA-15. This is evident from the collapsed silica channels and their distinct lack of order, presumably caused by the structure degradation cited here.

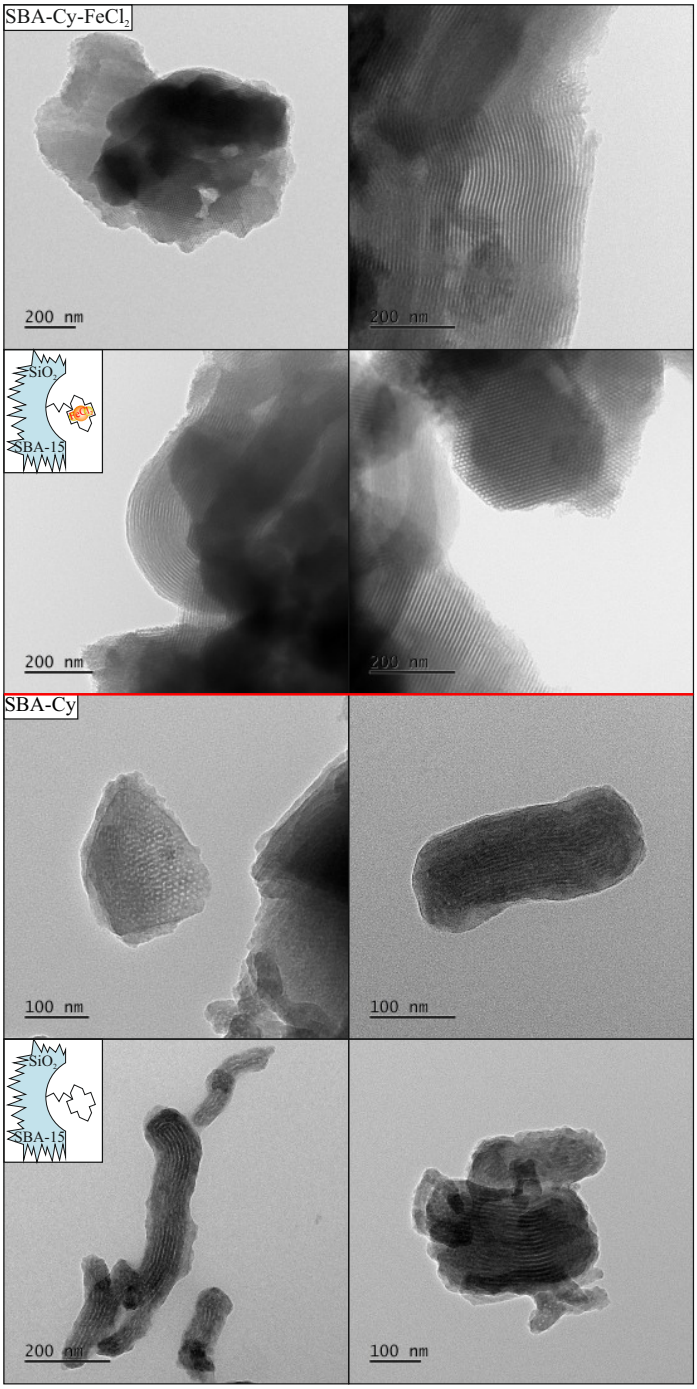

Figure 4: Tansmission electron microscopy images of SBA-15 silica containing iron chloride chelated by cyclam inside the pores – SBA-Cy-$FeCl_2$ (top) and SBA-15 silica containing only cyclam inside the pores – SBA-Cy sample (bottom).

The degradation of the structure of the material containing only cyclam, without the chelated metal compound cited above, is also confirmed by X-ray studies (Figure 5).

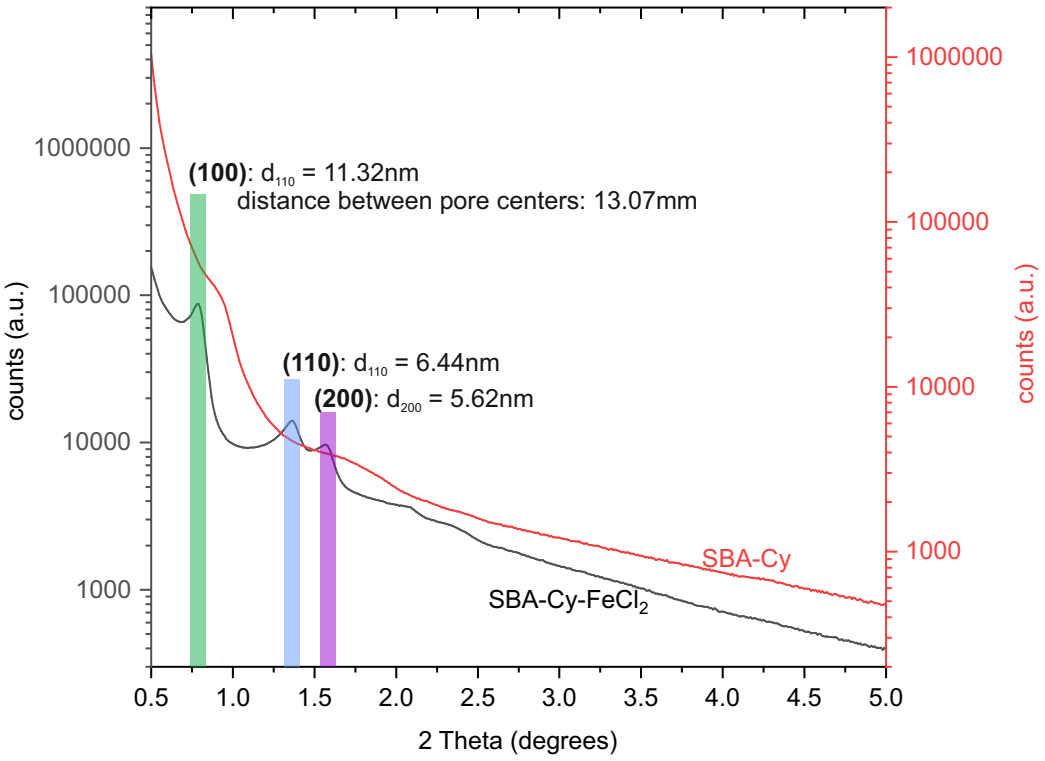

Figure 5: The small angle X-ray diffraction pattern for SBA-15 mesoporous silica functionalized by iron chloride chelated by cyclam inside the pores – SBA-Cy-$FeCl_2$ (black line) and SBA-15 silica containing only cyclam inside the pores – SBA-Cy sample (red line).

For the SBA-15 mesoporous silica functionalized by iron chloride chelated by cyclam inside the pores, the diffraction pattern consists of three peaks corresponding to the (100), (110), and (200) planes. They are specific for the hexagonal order of the pores in SBA-15 silica [30]. This proves that the SBA-Cy-$FeCl_2$ sample has a correct SBA-15 structure, undisturbed by the functionalization process. The calculated interplane distances and periodic distances between pore centers are given in Figure 5. In contrast, the peaks characteristic of the SBA-15 structure are virtually invisible in the SBA-Cy sample. Only a very broad feature for the 2Θ angle between 0.8 and 1.0

can be noticed, and second, even broader at the 2Θ region between 1.5 and 2.0. This fact may prove that the two-dimensional ordered structure of the silica matrix has been lost. The above-mentioned features are the remnants of peaks originating from the (100), (110), and (200) planes. Those bumps are slightly shifted toward higher angles, thus indicating the collapse of the structure (reduction of interplane distances).

Supplementary information for all structural data was provided by nitrogen sorption analysis. The nitrogen adsorption-desorption test was conducted to provide information about the porosity of the samples and their changes with the introduction of $FeCl_2$. In order to better understand the structural changes occurring in the sample containing only cyclam, we also analyzed the precursor sample of the sample with cyclam: silica SBA-15 containing chloropropyl groups (SBA-Cl).

The BET surface area of the SBA-Cy-$FeCl_2$ sample was $761 m^2 g^{-1}$, while the pore size was 6.3nm with a very narrow pore size distribution (obtained from the Barret-Joyner-Halenda equation, as can be seen in Figure 6). The curve obtained for the SBA-Cl reference sample has very similar characteristics. In this case, we got a specific surface area equal to $851 m^2 g^{-1}$ and a pore size of 6.6nm, also with a narrow pore size distribution. Difference in adsorption-desorption curves in high relative pressure can be related to the presence of cyclam groups with $FeCl_2$ inside pores which can decrease total pore volume and specific surface area. This fact also explains the slightly larger pore diameter for the SBA-Cl sample. Both samples mentioned present typical IV isotherms with a parallel H1 hysteresis loop, typical for SBA-15-type mesoporous materials [31, 32].

Silica containing only cyclam (SBA-Cy) shows different characteristics (Figure 6). Its specific surface area is much smaller, and its pore diameter distribution is much more blurred than that of a sample containing ferric chloride (with specific surface area $400 m^2 g^{-1}$ and average pore diameter 6.7nm). What is more, the adsorption-desorption curve lies below those measured for SBA-Cl and SBA-Cy-$FeCl_2$ samples. This fact is probably due to the disappearance of microporosity due to the degradation of the silica structure. Also, the adsorption and desorption branches of isotherm of SBA-Cy are not close (also in the range of 0.05-0.64 relative pressure) probably due to the destruction of silica walls and the presence of pore space interconnectivity [33]. All of this is indicative of the sample's degradation under atmospheric conditions.

Further research revealed the detailed molecular structure of the samples.

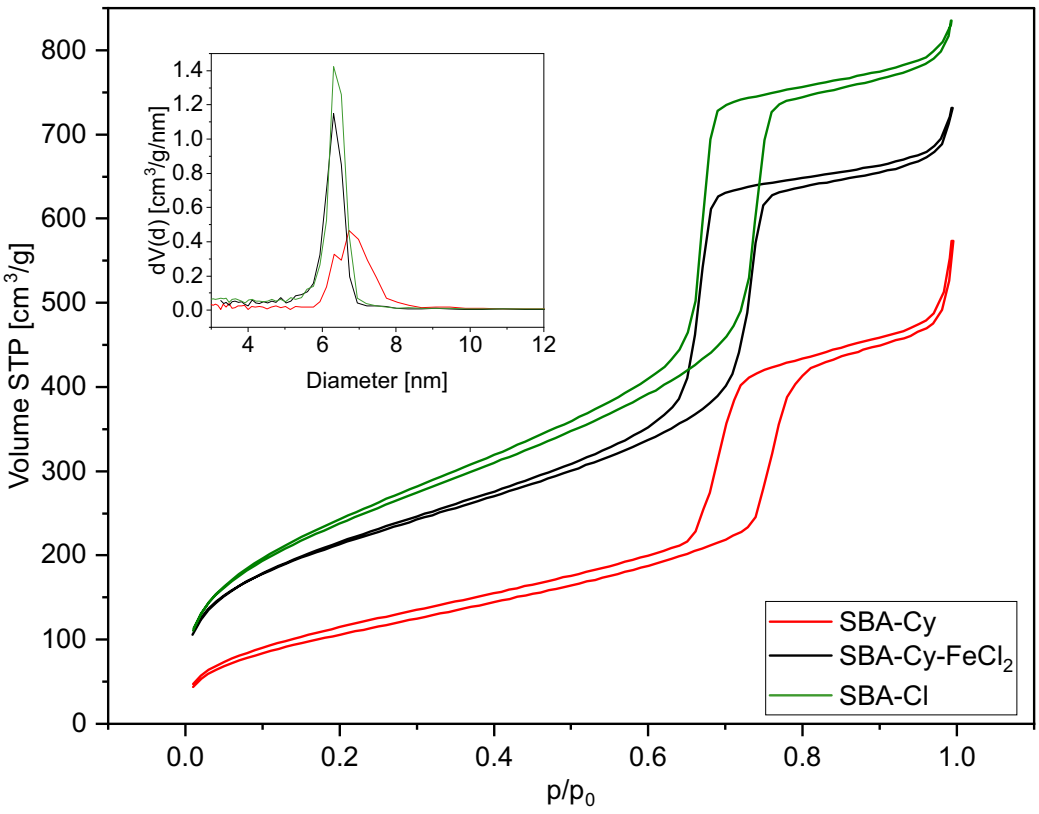

Figure 6: Nitrogen adsorption–desorption isotherms recorded for SBA-15 mesoporous silica functionalized by iron chloride chelated by cyclam inside the pores – SBA-Cy-$FeCl_2$ (black line), SBA-15 silica containing only cyclam inside the pores – SBA-Cy sample (red line), and SBA-15 containing chloropropyl units – SBA-Cl (green line), together with the pores sizes distributions obtained from the Barret-Joyner-Halenda equation (inset).

Raman spectroscopy was employed to systematically track the structural alterations within the silica network resulting from SBA-15 pore wall functionalization with cyclam and to confirm the sorption potential of cyclam through the activation of the composite with iron(II) chloride. This comprehensive approach involved the analysis of three distinct SBA-15-based specimens' spectra, allowing for a detailed structural examination (see Figure 7). Additionally, Raman spectra of SBA-Cy-$FeCl_2$ were compared to reference bulk $FeCl_2$ chelated by cyclam (Cy-$FeCl_2$) to validate the assumed sorption potential while considering the structure of SBA-15, the method of pores

interior functionalization, and the sorption properties of cyclam [34, 35].

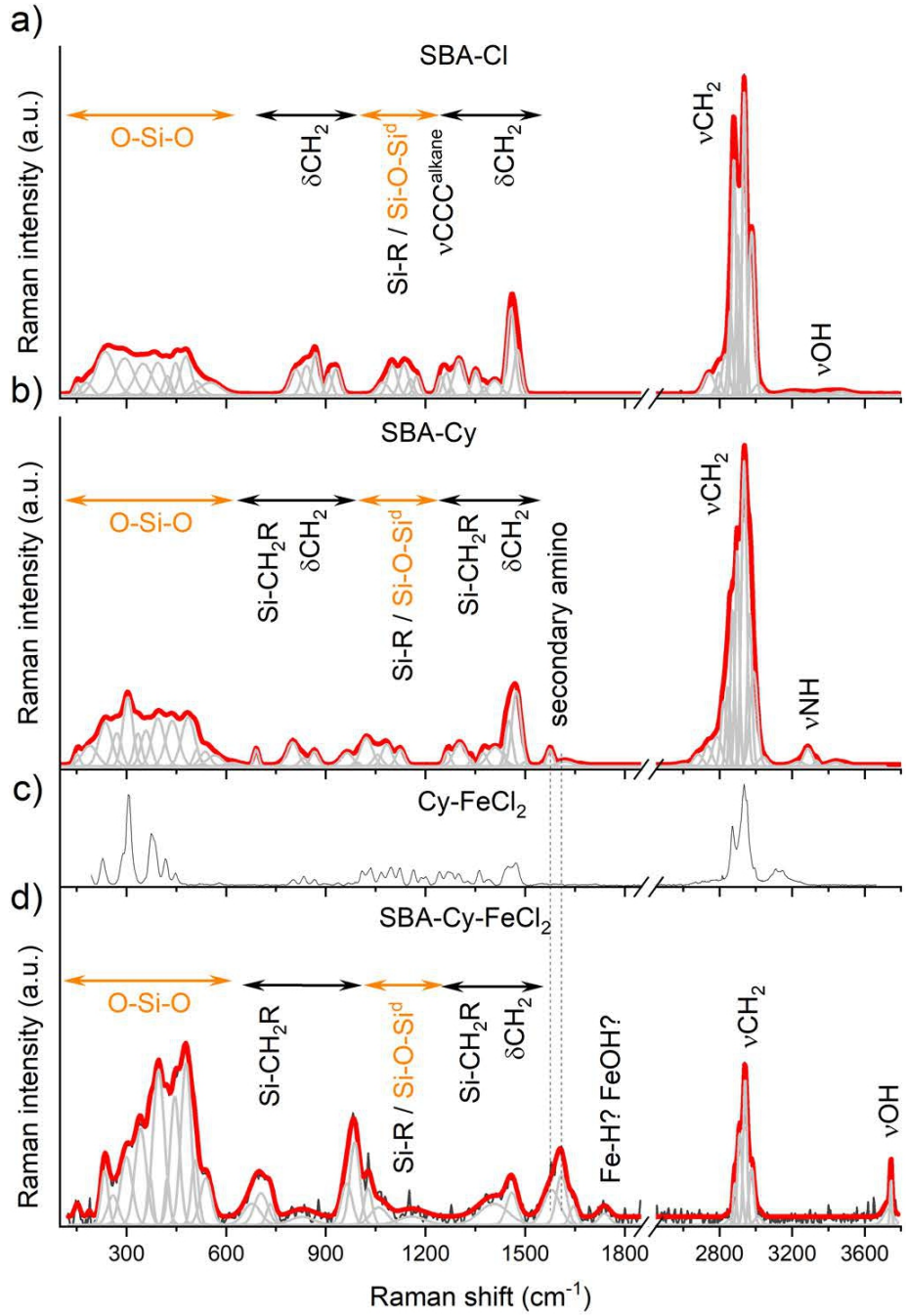

Figure 7: Raman spectra of SBA-15 mesoporous silica functionalized by chloropropyl units – SBA-Cl (a), cyclam – SBA-Cy (b), bulk $FeCl_2$ chelated by cyclam – Cy-$FeCl_2$ (c), and silica functionalized by iron chloride chelated by cyclam inside the pores – SBA-Cy-$FeCl_2$ (d). Spectra were summarized in the 100 – 3800cm^{-1} range and fitted using the Voigt function to recognize band positions by highlighting the vibration of individual molecular fragments.

The Raman spectra of the investigated silica-based samples were divided into two spectral regions: (1) 3800 — 2650cm^{-1} and (2) 1850 — 120cm^{-1} (Figure 7). The first region provided insights into the hydrophilicity of the system, signifying the presence of hydroxyl groups or molecular water. In turn, the latter region featured a band arrangement involving i) stretching and deformational modes within chloropropyl chains overlapping with similar stretching and deformational groups within macrocyclic ligand and complex (1800 – 1250cm^{-1}), ii) silicon-oxygen tetrahedral modes (1250 – 850cm^{-1}) overlapping with deformational vibration of macrocyclic ring molecular structure (1350 – 800cm^{-1}) as well as iii) the medium-range order silica vibrations corresponded with lattice defects (850 - 150cm^{-1}).

In this context, the Raman spectra of all composites in the first region exhibited dominant bands with maxima at 2930 and 2880cm^{-1} corresponded to ν_{as} and $\nu_s CH_2$ originating from the asymmetric and symmetric stretching modes of CH_2 groups within propyl chains (inside SBA-15 channels) and the macrocyclic ring of cyclam (cyclam-containing samples). The complex arrangement of bands observed for SBA-15-derived indicated a high conformational diversity of propyl chains, further affirming the correctness of silica pore wall functionalization. Incorporating cyclam into the silica carrier marginally altered the band arrangement in the region (1), especially concerning the number and intensity of CH_2 bands. This change resulted from the structural modification of propyl chains. It implied the formation of macrocyclic ring cyclam anchored to the propyl chains (cyclam substituted Cl atom at the end of the -Si-propyl chain). A similar CH_2-band arrangement was observed after chelating iron chloride by cyclam in SBA-Cy-$FeCl_2$ sample, where the bands' intensity was reduced several times, confirming the formation of metal complexes [36].

Furthermore, the spectra of SBA-15-derived samples (especially SBA-Cl) exhibited weak bands with maxima around 3465 and 3208cm^{-1}, confirming the presence of hydroxyl groups or molecular water. Incorporating cyclam and the confinement effect within the silica pore walls revealed an additional band of around 3282cm^{-1}, related to the symmetric νNH stretching vibration of secondary amino groups. It may suggest the coexistence of cyclam in various configurations (see: further discussion in section 4).

The Raman spectrum of the iron chloride-cyclam chelated system displayed a similar CH_2+NH-related band arrangement. However, the amino groups exhibited downshifts to lower frequencies due to the chelation nature and interaction with iron. Two amino bands around 3150 and 3105cm^{-1}

resulted from free NH and inter- or intra-hydrogen bonded amino groups, reflecting the variable conformation of metal-doped cyclam [37]. Introducing iron chloride salt to the functionalized silica pores slightly modified the spectral pattern. The Raman spectrum of SBA-Cy-$FeCl_2$ showed the absence or substantial weakening of amino-related bands and the appearance of a band at 3730cm^{-1}, linked to the stretching vibration of hydroxyl units (see Figure 7). This effect was hypothesized to result from the complexation nature of cyclam, which weakened the N-H bonds by enhancing the Fe–N bond [36, 38, 39]. This complexation led to structural rearrangements and conformational transformations of the cyclam macrocyclic ring enforced by its interaction with iron. Consequently, the more mobile cyclam moieties within the pores reorganized into a mixture of cis/trans forms, with varying iron sorption potential, resulting in the formation of oxygen–oxygen bond-stabilized complexes $[Fe^{V}(cyclam)(O)_2]^+$ and $[Fe^{V}(cyclam)(OH)(O)_2]^+$ [40].

Raman spectra of all SBA-derived samples in the latter region featured a band arrangement involving i) stretching vibration of alkane C-C and deformational CH_2 groups within propyl chains overlapping with stretching alkane ν(CC+CN) and deformational methylene and amino groups within macrocyclic ligand and complex (1800 – 1250cm^{-1}), ii) silicon-oxygen tetrahedral modes (1250 – 850cm^{-1}) overlapping with deformational (1350 – 800cm^{-1}) as well as iii) the medium-range order silica vibrations corresponded with lattice defects (850 – 150cm^{-1}) [40, 37].

In greater detail, the fingerprint region spanning from 1850 to 1250cm^{-1} exhibited numerous bands attributed to the bending of -CH_2- groups overlapping with skeletal C-C stretching vibrations within the propyl chain and confirms its presence in both SBA-Cl and SBA-Cy samples [41]. However, the introduction of the cyclam ligand into the interior of the pores led to the appearance of a weak band around 1563cm^{-1} and a slight modification in band intensities between 1480 – 1420cm^{-1}. These changes resulted from the activation of deformation δNH, asymmetric and symmetric deformation δCH, and stretching νCC and νCN modes within the macrocyclic ring due to the presence of cyclam [42, 36, 43].

Interestingly, the Raman spectrum of cyclam-containing SBA-15 shows a shift in the N-H band compared to available literature data, indicating variable conformations of the cyclam ligand and confirming the postulated variable anchoring to the propyl chains (Figure 7). The band arrangement in the cyclam complex exhibited a downshifted and weakened intensity of the δNH band characteristic for a trans conformed [42, 36, 43, 38]. In addition,

the second δNH band seemed to be upshifted and increased in intensity, suggesting the complexation of iron through the *cis*-cyclam conformer, change in the iron valency, and $[Fe^{V}(cyclam)(O)_{2}]^{+}$ and $[Fe^{V}(cyclam)(OH)(O)_{2}]^{+}$ complex formation in the presence of hydroxyl or water molecules [40]. An alternative hypothesis assumed a proton exchange mechanism within the iron complex system as N-H-$\cdots$Fe, activating the Fe–H species [44]. In both hypothetical scenarios, three bands appeared in the Raman spectrum around 1654, 1632, and 1725cm^{-1} may originate from Fe-X (X = -H, -OH, - H_2O) overlapping with deformational CH_2 modes within $[Fe(cyclam)]^{2+}$ cation [45]. It's worth noting that the typical bands of Si-propyl chains exhibit weakened intensities and are masked, confirming the formation of the cyclam complex (Figure 7).

The nature of other bands, particularly those falling within $1250 - 850$cm^{-1} range, was notably intricate due to overlapping vibrations originating from various molecular fragments of the functionalized composite, including stretching Si-O-Si modes within the silica network [46, 47], symmetric deformation of long aliphatic chain in Si-C_xH_y, as well as stretching and deformational modes of ν(CC+CN), δ(CH_x+NH) [38, 48].

In the context, the Raman spectrum of chloropropyl-functionalized SBA-15 (SBA-Cl) featured four bands at 1180, 1135, 1100, and 1075cm^{-1} attributed to the overlapping asymmetric SiO_2 (Q4) vibrations in fully polymerized silica structures [49, 50, 51] with asymmetric stretching Si-C vibrations, confirming the presence of propyl chains tailored to the silica pore walls [52].

On the other hand, Raman spectra of cyclam-functionalized silica, contrary to this observed on the SBA-Cl spectrum, displayed two additional bands with maxima around 1024 and 950cm^{-1}, suggesting lowering of silica network ordering during synthesis in the presence of cyclam-anchoring reagent. Unfortunately, the nature of such bands was complicated because of the coexistence of symmetric stretching vibrations of the terminal oxygen atoms of SiO_4 tetrahedra with one or two non-bridging oxygen molecular fragments (NBO) [53, 54], as well as deformational modes of δNH and ρCH within the macrocyclic ring of the ligand [43, 39, 48].

Interestingly, functionalization of SBA by cyclam led to a significant increase in band intensity around 950cm^{-1} and a reduction of other bands above 1100cm^{-1}, while the observable effect amplified by the confinement effect correlate with alterations in the lone pair electron availability within the ring caused by iron complexation [43, 42]. The latter effect additionally explained

the progressive reduction of bands related to the deformational CH_2 modes of propyl observed in the 925 -– 850cm^{-1} (Figure 7).

The band arrangement at lower frequencies below 650 cm^{-1} within all functionalized SBA-15-based samples provided insights into the O-Si-O bending motion of n-membered silica rings, where n can be 3, 4, 5, 6, etc. [55]. The complexity of these bands was further associated with the modification of the silica network resulting from the incorporation of propyl inside silica pores, which enhanced the formation of structurally defective fragments such as $Si_2O_6^{4-}$ and $Si_2O_5^{2-}$. A similar band arrangement was observed for SBA-Cl and SBA-Cy, with the latter displaying a new band around 687 cm^{-1}, indicating the formation of an additional $Si_2O_7^{6-}$ molecular unit [56].

Iron chloride salt introduced into the interior of the silica pore enforced structural rearrangements and enhanced the intensity of the $Si_2O_7^{6-}$ [56] band. Furthermore, according to literature, metal complexation activates bands related to stretching νFeN modes with deformation involving the metal atom, which on the Raman spectrum of Cy-$FeCl_2$ appeared at 445, 415, and 225cm^{-1} [57, 43]. On the other hand, the Raman spectrum of Cy-$FeCl_2$ highlighted strong bands at 380, 310, and 285 cm^{-1} indicating symmetric stretching modes of linear $FeCl_2$ complexes, charged $FeCl_x^{2-x}$ complexes with explicit H_2O solvation, and hydrated charged $FeCl^{2+}$ complexes [58, 59, 60] (Figure 7). However, due to the confinement effect and the predominant impact of silica in SBA-Cy-$FeCl_2$, those modes overlapped with O-Si-O vibrations, making it challenging to confirm iron chloride complexes directly. An alternative explanation corresponded to the system's relatively low potential to entrap iron chloride in the macrocyclic ring due to the coexistence of cis/trans cyclam conformations. Hence, trans conformers tend to complex iron and iron chlorides. In contrast, cis conformers with the presence of hydroxyl and/or water molecules present within the interior of the pore walls enforced iron oxidation and the formation of $[Fe^{V}(cyclam)(O)_2]^+$ and $[Fe^{V}(cyclam)(OH)(O)_2]^+$ complexes [40]. Such complexes, through a proton-coupled electron transfer process yielded conversion to $Fe^{V}(O)(OH)$, which, in the presence of saline conditions [61], crystallizes into oxyhydroxides with chlorine incorporated into the tunnel structure of β-FeOOH akagenaite [62, 63, 64]. We have found such nanocrystals in some parts of the SBA-Cy-$FeCl_2$ sample – see: Figure 8. Here, we must remark that it is possible that their visibility is related to the surface amplification of the signal by the silica walls between which the crystals are located, so the signal is disproportionate to their quantity [65].

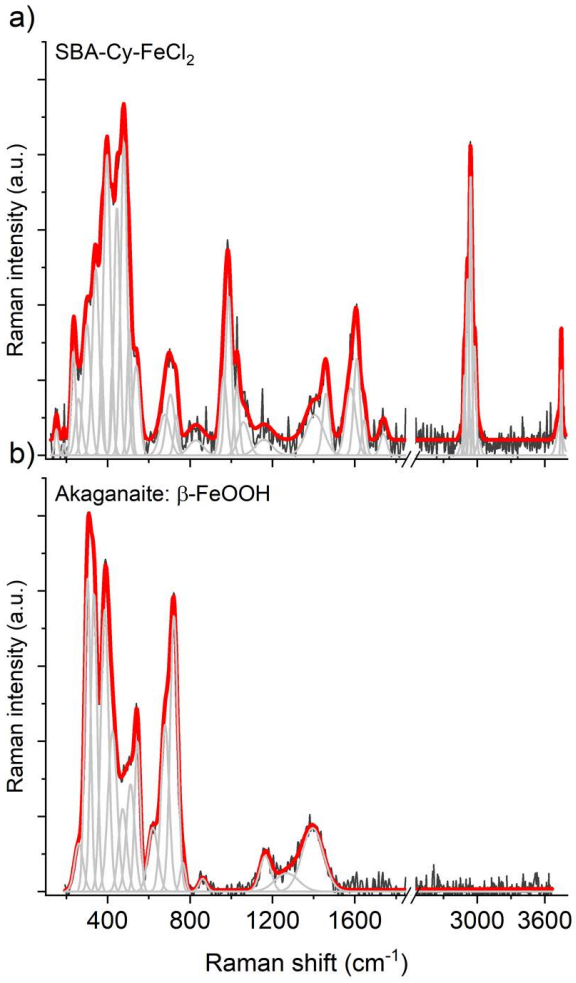

Figure 8: Raman spectra of iron-activated SBA-15 sample (SBA-Cy-$FeCl_2$) gathered from variable places of the samples (A, B), showing some remaining β-FeOOH akagenaite crystals occurring in the sample. Spectra were summarized in the 100 — 3800 cm^{-1} range and fitted using the Voigt function to recognize accurate band positions with highlighting vibration of individual molecular fragments.

The SBA-Cy-$FeCl_2$ sample was examined using Time-of-Flight Secondary Ion Mass Spectrometry. This technique allows analysis of the upper layers of the material's surface (1-3 nm). In addition, it provides information on both atomic and molecular ions [66], and is also used to study catalysts [67].

Analysis of the carbon-containing fragments indicates the presence of cyclam and organic bonding directly to the silicon atom, as we would expect from a synthesis procedure. Examples of the ions analyzed are: CH_2^+ (m/z 14.01), CH_3^+ (m/z 15.02), CHN^+ (m/z 27.01), $C_2H_3^+$ (m/z 27.02), CH_2N^+ (m/z 28.01), $C_2H_4^+$ (m/z 28.02), $C_2H_5^+$ (m/z 29.03), $C_3H_3^+$ (m/z 39.02), $SiCH_2^+$ (m/z 41.99), $C_2H_4N^+$ (m/z 42.03), $C_2H_5N^+$ (m/z 43.04), $C_3H_7^+$ (m/z 43.05), $C_3H_6N^+$ (m/z 56.05), $C_3H_5N_2^+$ (m/z 69.05), $C_4H_8N^+$ (m/z 70.07), $C_3H_7N_2^+$ (m/z 71.06), $C_4H_5N_2^+$ (m/z 81.04), $C_4H_7N_2^+$ (m/z 83.06), $C_4H_9N_2^+$ (m/z 85.07), $C_5H_7N_2^+$ (m/z 95.05), $C_5H_9N_2^+$ (m/z 97.07), $C_6H_{12}N^+$ (m/z 98.09), CH_2^- (m/z 14.02), NH^- (m/z 15.01), C_2H^- (m/z 25.01), CN^- (m/z 26.00), $CNCl^-$ (m/z 60.97) and CCl^- (m/z 46.96). It was not possible to find a fraction containing C-C-C-N-C-C-C-N-C-C-C or similar fragments to confirm that the cyclam ring is anchored in at least 2 places.

Of interest is the SiH-textsuperscript+ ion (m/z 28.98) confirmed by the isotope effect (signals at: 28.9842 $^1H^{28}Si^+$, 29.9848 $^1H^{29}Si^+$, 30.9810 m/z $^1H^{30}Si^+$ in proportions 1:0.05:0.03). The SiH-textsuperscript+ bond should not be present in the sample due to the method of synthesis. It was probably formed from the decomposition of the Si-CH fragment$_2$.

Ion fragments containing silicon and carbon show direct bonding of the carbon chain to silicon, e.g.: $SiCH_2^+$ (m/z 41.98). Other silicon-containing ion fragments are typical of silicas, for example: SiO_2^- (m/z 59.97), $Si_3HO_7^-$ (m/z 196.90), $Si_4HO_9^-$ (m/z 256.86), and $Si_5HO_{11}^-$ (m/z 316.82).

Fragments containing an iron atom were also found on the spectra: Fe^+ (m/z 55.93), FeH^+ (m/z 56.94), FeO^+ (m/z 71.92), $FeOH^+$ (m/z 72.94), $CHNFe^+$ (m/z 82.94), CH_2NFe^+ (m/z 83.95), $FeCl^+$ (m/z 90.90) $C_2H_4NFe^+$ (m/z 97.97), $FeNH^-$ (m/z 70.95), FeO^- (m/z 71.92), FeO_2^- (m/z 87.91), $FeCl^-$ (m/z 90.90) and $FeCl_2^-$ (m/z 125.86). The fragments listed indicate that, the iron atom is in close proximity to the cyclam. No fragments of Fe with SiO were found, or their intesiveness is negligibly low, which shows that the iron atoms are mainly in a complex together with cyclam. In addition, fragments containing chlorine show that this atom is found in close surroundings of both the iron atom and the cyclam. Noteworthy ions are: $Fe_3O_3^+$ (m/z 215.78), $Fe_4O_4^+$ (m/z 287.70), $Fe_5O_5^+$ (m/z 359.64), $Fe_6O_6^+$ (m/z 431.56), $Fe_7O_7^+$ (m/z 503.50), $Fe_8O_8^+$ (m/z 575.41). Despite the fact that the signal

intensity is four orders of magnitude lower, I show that the β-FeOOH clusters of akagenaite containing at least z 1-8 Fe atoms are incipient. The presence of akagenaite was also observed on Raman spectra.

An analysis of the maps provided by ToF-SIMS provides interesting information. An example can be found in Figure 9. It shows that there is a uniform distribution of the cyclam system in the test tube, probably cyclam complexes are also present on the surface of the spatial silica structure. It can be seen from the distribution of iron ions that akagenaite contamination is local.

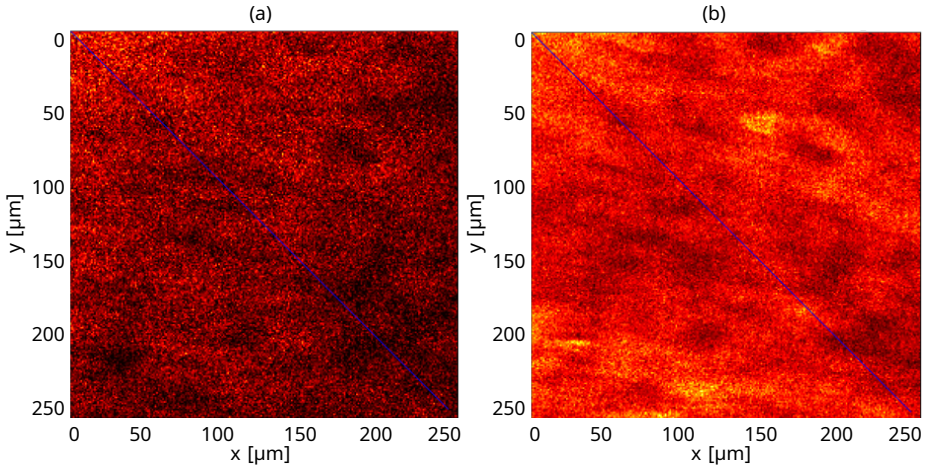

Figure 9: Time-of-flight secondary ion mass spectrometry (ToF-SIMS) overlap maps of distribution of NH_3^+, NH_4^+, NH_2^+ (a) and Fe^+, FeH^+, FeC^+, $FeOH^+$, $FeOH^+$, $FeOH_2^+$, Fe_2N^+ (b).

On the basis of experimental and previous data, we prepared the model containing a fragment of the silica wall and a cyclam ring (see: Figure 10). After optimization, it can be clearly seen that there are classical Si-O-H$\cdots$O hydrogen bonds on the silica wall ($l_{\mathrm{H}\cdots\mathrm{O}}$ = 1.8 to 2.1 $\mathring{A}$, α_{OHO} 140-170°). The cyclam, together with the $FeCl_2$ ion, is located on the silica wall, as there is additionally an O-H$\cdots$Cl interaction. ($l_{\mathrm{Cl\text{-}H}}$ = 2.16Å, $\alpha_{\mathrm{Cl\ H\ O}}$=172°). Interactions of this type in solvents have been discussed for five decades. This means that it can be concluded that the Cl...H-O interaction is certainly not purely electrostatic, but shows all the features of a "standard" hydrogen bond [68].

Stabilization of the cyclam ring with $FeCl_2$ also explains the clearer signals on the XRD spectrum for the sample with metal than for SBA-Cy alone. From the cell distance analysis, it is clear that the channel in the silica is large enough that placing the ions together with the cyclam will disrupt its diameter by only a few percent.

The second model that was prepared is a cyclam with four N-propyl groups, illustrating the possibility of anchoring the cyclam in four places (see: Figure 10, right model). The sizes and Si:Cyclam ratio shows that it will be very difficult to create even two anchorages.

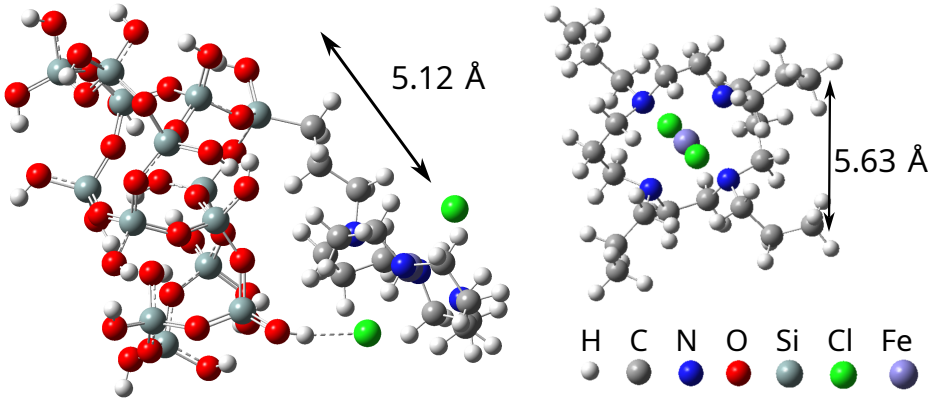

Figure 10: Numerical model of SBA-Cy-$FeCl_2$ and cyclam with four N-propyl groups

Magnetic measurements, conducted over a broad temperature range, unveil compelling insights into the magnetic properties of the SBA-Cy-$FeCl_2$ (as illustrated in Figure 11 with an upper inset). The striking magnetic order, most evident during magnetization measurements performed without an external magnetic field, is particularly noteworthy, displaying a spontaneous magnetization characteristic. Of particular note was the pronounced magnetic order, which was most conspicuous during magnetization measurements performed without an external magnetic field, manifesting a distinctive and spontaneous magnetization characteristic.

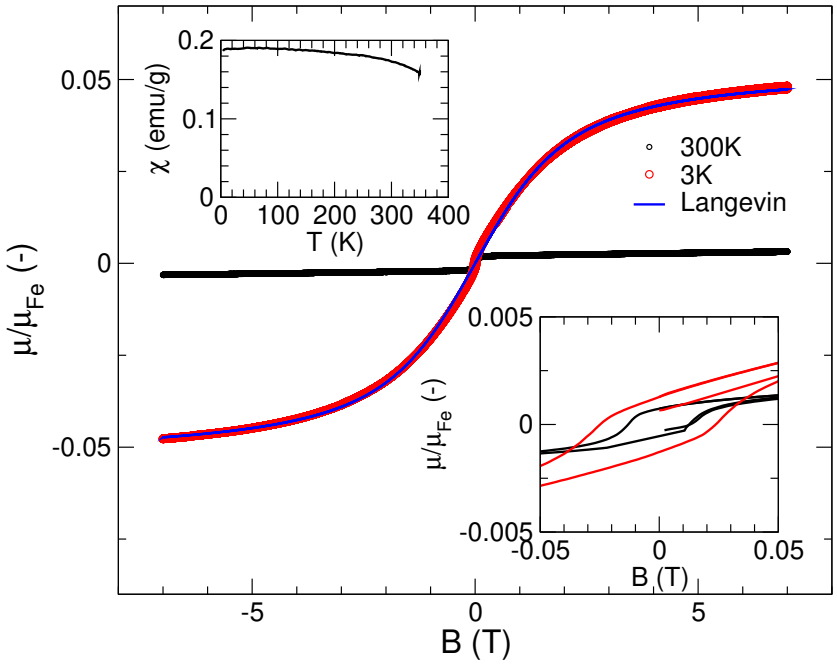

Figure 11: Magnetic measurements performed for the SBA-Cy-$FeCl_2$. Data summarized at 3K and 300K. Two insets illustrate the magnetization χ of the sample vs. temperature T (upper inset) and magnetization at a low magnetic field with a hysteresis loop typical for a ferromagnet.

The magnetization behavior at low magnetic fields revealed a hysteresis loop that provides unequivocal evidence of the sample's ferromagnetic nature, stemming from the presence of iron. Specifically, at room temperature, the hysteresis loop exhibits a width of approximately 30mT, which expands to nearly double that width at 3K. As a result, temperature-dependent magnetization behavior was fitted using the Langevin curve defined as

$$m(x) = \alpha L(\beta x) \tag{1}$$

where

$$x = \frac{\mu_0 H}{k_B T} \tag{2}$$

and

$$L(x) = \coth(x) - 1/x \tag{3}$$

with k_B representing the Boltzmann constant, H signifies the magnetic field, and T represents the sample temperature. As a result of the fitting procedure, the remarkable agreement between experimental data and the theoretical model at low temperature (T = 3K) resulted in robust fit parameters of $\beta = 1.219$ and $\alpha = 0.0535$ signifies the maximum iron content ($\sim 5.35\%$) in the sample of the overall sample mass. Notably, at room temperature, the magnetization, represented on the y-axis as a fraction of the magnetization of bulk iron at room temperature (217emu/g), was found as only 0.31% of the value one would anticipate for bulk iron.

The discrepancy between the low-temperature and room-temperature data can be attributed to the distribution of iron within the sample, which was related to the occurrence of iron in the form of particles of varying sizes. Notably, a minor fraction of the iron in the sample, constituting only about 5.8% of the whole iron 0.31% by weight of the sample, taking into account the total mass content of iron of 5.35%.), comprises larger iron particles exceeding the superparamagnetic limit with ferromagnetic order at room temperature. Larger particles resulted from akageneite structure crystallized within the silica interior. In turn, the predominant portion of the iron exists as smaller particles, falling below the superparamagnetic limit, suggesting the complexation of iron by the macrocyclic ring.

4. Discussion

Structural studies have clearly shown that the material functionalized with iron chelated by cyclam retains the correct structure of two-dimensionally

ordered SBA-15 silica after one month of aging. However, the structure degrades after this time of aging in the case of material containing only cyclam. In order to better analyze the stability of the material containing sole cyclam over time, we juxtaposed the structural results of this nanocomposite performed just after synthesis and after one month of aging. A comparison of the SEM, TEM, XRD and nitrogen sorption analysis results is shown in Figure 12. The material containing the iron(II) chloride chelating cyclam did not show structural differences when tested just after synthesis and after one month of aging, so it was omitted from this comparison.

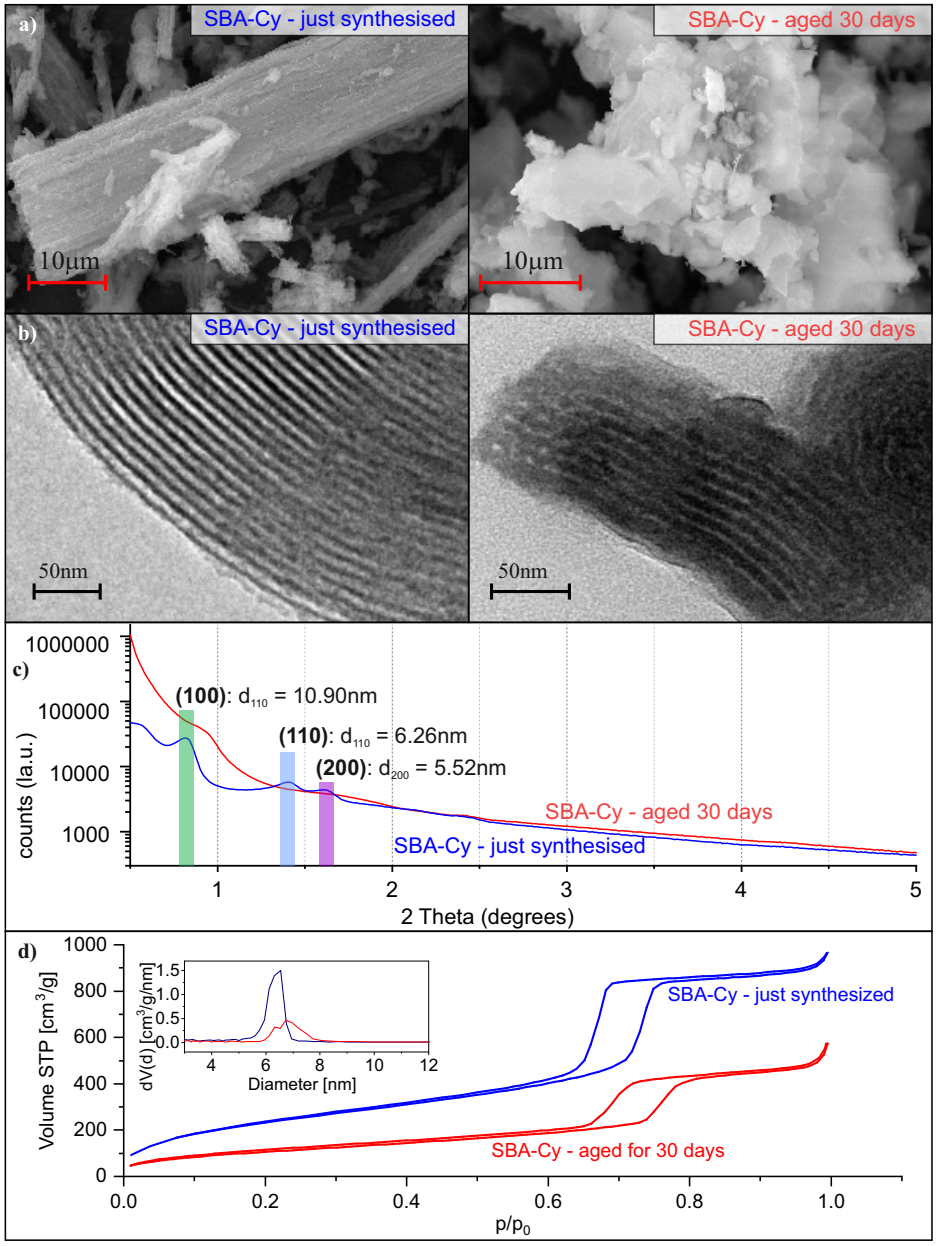

Figure 12: Juxtaposition of the structural investigations results for the SBA-15 silica containing sole cyclam inside the pores: juxtaposition results for the material just after the synthesis and aged for 30 days. Scanning electron microscopy (a), transmission electron microscopy (b), small angle X-ray diffractometry (c), and N_2 sorption analysis (d).

Closely inspecting the scanning electron microscopy images (Figure 12a) reveals some apparent differences between the samples. Looking at the left photo, showing just-synthesized SBA-Cy, the material looks like typical SBA-15 silica with the characteristic long grains of [69]. In contrast, the photo on the right, presenting the same material after 30 days of aging, shows the material without the visible grains, characteristic of SBA-15. This may indicate its degradation over time, resulting in the structural collapsing of whole silica grains. Similar conclusions within the microstructure can be drawn by comparing TEM images of both samples considered here (Figure 12b). Just-synthesized SBA-Cy (Figure 12b left side) presents the well-defined structure of the SBA-15 silica, with its characteristic channels arranged in an ordered 2D hexagonal pattern [28, 29]. After 30 days of aging, the structure of the sample changes noticeably (Figure 12b right side, see also Figure 4). The structure of the pores expressly collapses, which is made evident by their irregular diameter (expressive constrictions inside the pores can be observed). Even more evident structural changes between the just-synthesized sample and the sample aged for 30 days are observed in the XRD spectrum (Figure 12c). Just synthesized SBA-Cy manifests typical features observed for SBA-15 silica with 2D hexagonally ordered pores in the low-angle region (described in detail in Section 3). After 30 aging, however, the pores ordering features disappear, as manifested by the disappearance of Bragg reflections originating from the 100, 110, and 200 planes. We can draw similar conclusions by analyzing nitrogen sorption for the samples compared here(Figure 12d). Just after synthesis, the SBA-Cy sample shows typical IV isotherms with a parallel H1 hysteresis loop, typical for SBA-15-type mesoporous materials [31, 32]. The BET surface area of the just synthesized sample was $784 m^2 g^{-1}$, while the pore size was 6.2nm with a narrow pore size distribution. Aging for 30 days, however, results in a change in the sorption characteristics of the material. The lowering of the position of the isotherm is the result of the disappearance of micro-porosity. Moreover, the specific surface area of the material has significantly decreased to $400 m^2 g^{-1}$, while the pore diameter distribution has been blured. In addition, adsorption and desorption curves do not coincide even in low ranges of relative pressures (what is more visible in Figure 6), which may indicate the occuring of interconnections between silica channels, due to degradation of its structure [33].

As can be seen, the structure of the SBA-15 silica containing sole cyclam inside the pores degrades over time. It is now well established that amino-functionalized silica gels suffer from poor chemical stability due to

nucleophilic assistance to hydrolysis [70, 71], and this is also true for cyclam-functionalized silica materials [72]. It is also known that amino-functionalized mesoporous silica materials undergo both chemical and structural damages, especially when contacting aqueous media, as a result of the alkaline properties of amino groups [72, 73]. This contributes to explaining why the SBA-Cy sample underwent structural degradation after aging for one month in the atmosphere (thus contacting humidity) as a result of pore walls collapsing. By contrast, the SBA-Cy-$FeCl_2$ material kept its good quality hexagonal mesostructured, which can be explained by the coordination of iron species to the nitrogen atoms of cyclam, forming a Cy-$FeCl_2$ complex in which the lone pairs on the nitrogen atoms are no more available for interacting with the silica structure. Indeed amino-functionalized silica materials anchoring metal ions (such as Hg(II) on aminopropyl-silica [74], or Ni^{2+}/Co^{2+}-cyclam modified mesoporous silica [75]) were characterized by much better chemical and/or structural stability than their non-complexed analogues. This is promising for ensuring long-term operational stability to the SBA-Cy-$FeCl_2$ material developed here.

Raman and ToF SIMS spectroscopies partially confirmed the assumed molecular structure. However, cyclam can be bound to silica walls in more than just the way assumed in the synthesis. The cyclam is deposited in channels and probably on the surface of silica pores. The optimized fragment of the structure (Figure 10) in which the ratio of Si ions to cyclam is 14:1 (in the assumed structure we have a ratio of 20:1, but due to computational complexity, the amount of silicon was slightly reduced) shows that the packing is high enough that it is possible to anchor the cyclam not only by one, but also by two propyl groups. It should be emphasized, however, that in order for a reaction to occur that will lead to the formation of an N-C bond from a C-Cl bond, there must be an appropriate approximation of sites. With the rigid position of the chloropropyl groups, which, however, are labile, such an arrangement is possible (in particular, that the chloropropyl groups are relatively abundant in the system). Nevertheless, it seems intuitively that a maximum of two cyclam anchor sites can be formed. The probability of anchoring a cyclam through three or four sites, as shown in Figure 13, is very low. ToF SIM studies also show that there are few fragments containing the C-Cl system. This could suggest that not all groups were substituted.

SQUID magnetometry, on the other hand, allowed quantitative estimation of the iron content of the samples. The study shows that the samples contain a total of 5.35 % iron, including 0.31 % bulk iron and 5.04 % iron

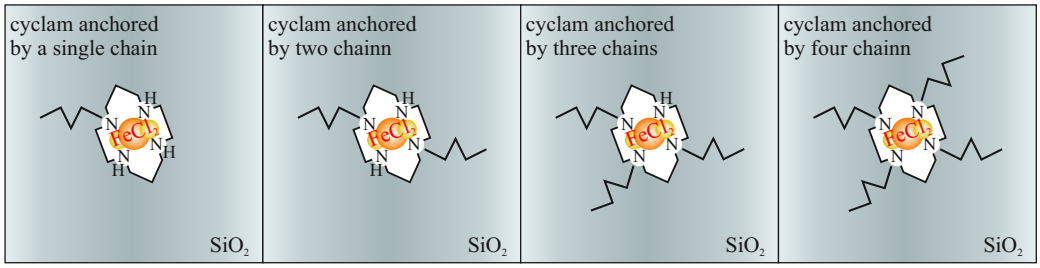

Figure 13: Possible ways to immobilize $FeCl_2$ chelated by cyclam in silica pores.

in a dispersed form, most likely in the form of ions chelated by cyclam. It should be remembered, however, that the mass iron content was estimated here, while in the synthesis process, we assumed molar ratios to SiO_2 groups. After converting the synthesis assumptions to mass ratios (also taking into account anchor groups and cyclam), the samples should contain 3.61 % iron. The amount of iron in the samples is, therefore, slightly higher than assumed. The bulk iron is probably a result of the formation of crystalline phases in the samples during synthesis. It should be remembered that anhydrous ferric chloride, used during synthesis, is extremely sensitive to moisture, and even using absolute alcohol and a protective atmosphere, we are not able to avoid partial conversion of iron to the hydrated form or its oxidation to iron(III). Such compounds can remain in the material in the form of nanocrystallites. The formation of akageneite nanocrystals is also possible under such conditions, as confirmed by Raman spectroscopy. However, the excess of iron in a dispersed form is a mystery to us. A plausible explanation could have been some excess cyclam bound to the silica surface in some way other than through propyl chains. Such groups could have chelated iron chloride, which is why such a significant amount of iron would be found in the sample.

The above conclusions are crucial for the potential applications of the material presented here, and especially for environmental applications. When designing the molecular structure of the presented nanocomposite, we assumed its application for water and soil treatment. Theoretically, placing a material with strong chelating properties and high adsorption capacity (related to the developed surface of the material), one can expect selective uptake of certain substances. In our case, we assumed the uptake of metal(II) ions and their chlorides.

However, the results of our study showed that the proposed material can

be used in environmental applications only to a limited extent. Its sorption properties were confirmed unequivocally. What's more, the amount of adsorbed metal (iron in this case) was even higher than assumed, and it was iron in a dissociated form, so most likely chelated by cyclam. However, the material, in the form containing only cyclam, is susceptible to degradation, which adversely affects its properties (reduction of specific surface area, confirmed by nitrogen sorption tests). Therefore, only fresh, just synthesized material is suitable for environmental applications.

The material containing iron(II) chloride, however, showed stability. Moreover, the study showed that the iron-containing functional groups were well separated from each other. It can, therefore, be assumed that the nanocomposite proposed here can potentially serve as an SAC. Of course, this thesis needs to be confirmed through catalytic testing, which will be the subject of further research.

5. Conclusion

In conclusion, in this article we have shown an efficient procedure for the synthesis of SBA-15-type porous silica functionalized with highly chelating cyclam molecules, which effectively bound iron chloride. By adopting a relatively low concentration of cyclam, anchored inside the silica pores with propyl groups, the material effectively separated individual $FeCl_2$ molecules inside the silica pores.

We observed significant differences between silica containing only cyclam in the pores, and the same material containing chelated iron (II) chloride. The differences were primarily in the stability of the materials. The iron-containing material showed correct stability, and its structure did not differ from standard SBA-15 silica, as shown by structural studies (SEM, TEM, XRD, and nitrogen sorption analysis).

In contrast, the material containing only cyclam was found to be unstable under atmospheric conditions. As shown by structural studies, the structure of SBA-15 degraded significantly over time as a result of nucleophilic hydrolysis support. The interaction of cyclam with iron(II) chloride molecules to form a Cy-$FeCl_2$ complex counteracted this situation, as lone pairs on nitrogen atoms are no longer available to interact with the silica structure. This has shown promise for ensuring the long-term operational stability of the SBA-Cy-$FeCl_2$ material developed here.

Spectroscopic studies (Raman and ToF SIMS) showed good agreement of the molecular structure of the obtained material with the assumptions of the synthesis. However, some discrepancies were obtained. It turned out that cyclam are not always anchored inside the silica channels with a single propyl chain. There is some probability of double anchoring of the cyclam group, with the connection of three or four propyl chains being rather unlikely. Moreover, crystalline phase intrusions into the material have been observed - crystallites of β-FeOOH akagenaite have been observed, probably forming during functionalization with ferrous chloride.

Magnetic studies, on the other hand, proved excellent separation of iron(II) chloride molecules and only a small inclusion of bulk material in the form of probably β-FeOOH akagenaite crystallites.

All this proved that the material we obtained had a molecular structure close to the assumption and good sorption properties. However, due to the instability of the form containing only cyclam inside the pores of SBA-15, such material is suitable for environmental applications only in just-synthesized form. However, after cyclam functionalization with ferric chloride, the material showed good stability. Given the good separation of iron-containing groups, its usefulness as a SAC can be considered.

6. Aknowledgement

This work has been supported by the resources of the National Science Centre: 2020/37/B/ST8/03637 (M.D. and Ł.L.), and 2021/43/D/ST8/00737 (M.L.).

The research was done within the framework of the POLONIUM project: BPN/BFR/2022/1/00003/U/00001 (A.W. and Ł.L.)

The authors are grateful to Poznan Supercomputing and Networking Center - PCSS for the opportunity to conduct numerical simulations.

References

[1] B. Qiao, A. Wang, X. Yang, L. F. Allard, Z. Jiang, Y. Cui, J. Liu, J. Li, T. Zhang, Single-atom catalysis of co oxidation using pt1/feox, Nature Chemistry 3 (8) (2011) 634–641. doi:10.1038/nchem.1095.
URL https://doi.org/10.1038/nchem.1095

[2] A. A. Herzing, C. J. Kiely, A. F. Carley, P. Landon, G. J. Hutchings, Identification of active gold nanoclusters on iron oxide supports for co oxidation, Science 321 (5894) (2008) 1331–1335. arXiv:https://www.science.org/doi/pdf/10.1126/science.1159639, doi:10.1126/science.1159639.
URL https://www.science.org/doi/abs/10.1126/science.1159639

[3] T. Imaoka, Y. Akanuma, N. Haruta, S. Tsuchiya, K. Ishihara, T. Okayasu, W.-J. Chun, M. Takahashi, K. Yamamoto, Platinum clusters with precise numbers of atoms for preparative-scale catalysis, Nature Communications 8 (1) (2017) 688. doi:10.1038/s41467-017-00800-4.
URL https://doi.org/10.1038/s41467-017-00800-4

[4] K. Xue, Y. Mo, B. Long, W. Wei, C. Shan, S. Guo, L. Niu, Single-atom catalysts supported on ordered porous materials: Synthetic strategies and applications, InfoMat 4 (6) (2022) e12296. arXiv:https://onlinelibrary.wiley.com/doi/pdf/10.1002/inf2.12296, doi:https://doi.org/10.1002/inf2.12296.
URL https://onlinelibrary.wiley.com/doi/abs/10.1002/inf2.12296

[5] B. Qiao, A. Wang, X. Yang, L. F. Allard, Z. Jiang, Y. Cui, J. Liu, J. Li, T. Zhang, Single-atom catalysis of co oxidation using pt1/feox, Nature Chemistry 3 (8) (2011) 634–641. doi:10.1038/nchem.1095.
URL https://doi.org/10.1038/nchem.1095

[6] T. Maschmeyer, F. Rey, G. Sankar, J. M. Thomas, Heterogeneous catalysts obtained by grafting metallocene complexes onto mesoporous silica, Nature 378 (6553) (1995) 159–162. doi:10.1038/378159a0.
URL https://doi.org/10.1038/378159a0

[7] M. Etienne, B. Lebeau, A. Walcarius, Organically-modified mesoporous silica spheres with mcm-41 architecture, New Journal of Chemistry 26 (4) (2002) 384–386.

[8] L. Laskowski, M. Laskowska, J. Jelonkiewicz, M. Dulski, M. Wojtyniak, M. Fitta, M. Balanda, Sba-15 mesoporous silica free-standing thin films containing copper ions bounded via propyl phosphonate units-preparation and characterization, Journal of Solid State Chemistry 241 (2016) 143–151.

[9] A. Walcarius, Electroinduced surfactant self-assembly driven to vertical growth of oriented mesoporous films, Accounts of Chemical Research 54 (18) (2021) 3563–3575.

[10] L. Laskowski, M. Laskowska, Functionalization of sba-15 mesoporous silica by cu-phosphonate units: Probing of synthesis route, Journal of Solid State Chemistry 220 (2014) 221–226.

[11] X. Liang, P. Sadler, Cyclam complexes and their applications in medicine, Chemical Society reviews 33 (2004) 246–66. doi:10.1039/b313659k.

[12] J. Cho, R. Sarangi, W. Nam, Mononuclear metal–o2 complexes bearing macrocyclic n-tetramethylated cyclam ligands, Accounts of Chemical Research 45 (8) (2012) 1321–1330. doi:10.1021/ar3000019.
URL https://doi.org/10.1021/ar3000019

[13] R. Zare-Dorabei, M. S. Darbandsari, A. Moghimi, M. S. Tehrani, S. Nazerdeylami, Synthesis, characterization and application of cyclam-modified magnetic sba-15 as a novel sorbent and its optimization by central composite design for adsorption and determination of trace amounts of lead ions, RSC Adv. 6 (2016) 108477–108487. doi:10.1039/C6RA21895D.
URL http://dx.doi.org/10.1039/C6RA21895D

[14] Sujandi, S.-C. Han, D.-S. Han, M.-J. Jin, S.-E. Park, Catalytic oxidation of cycloolefins over co(cyclam)-functionalized sba-15 material with h2o2, Journal of Catalysis 243 (2) (2006) 410–419. doi:https://doi.org/10.1016/j.jcat.2006.08.010.
URL https://www.sciencedirect.com/science/article/pii/S0021951706002855

[15] B. Drahoš, P. Antal, I. Šalitroš, R. Herchel, Magnetic properties of fe(ii) complexes of cyclam derivative with one p-aminobenzyl pendant arm, Metals 10 (3) (2020). doi:10.3390/met10030366.
URL https://www.mdpi.com/2075-4701/10/3/366

[16] L. Zhang, Y. Ren, W. Liu, A. Wang, T. Zhang, Single-atom catalyst: a rising star for green synthesis of fine chemicals, National Science Review 5 (5) (2018) 653–672. arXiv:https://academic.oup.com/nsr/article-pdf/5/5/653/31569341/nwy077.pdf, doi:10.1093/nsr/nwy077.
URL https://doi.org/10.1093/nsr/nwy077

[17] S.-Y. Chen, M. Nishi, A. Chang, W.-C. Hsiao, T. Mochizuki, H. Takagi, C.-M. Yang, Well-ordered cs–ru/@sba-15 nanocomposite materials for low pressure ammonia synthesis, Sustainable Energy Fuels 4 (2020) 5802–5811. doi:10.1039/D0SE01077D.
URL http://dx.doi.org/10.1039/D0SE01077D

[18] M. Mureddu, F. Ferrara, A. Pettinau, Highly efficient cuo/zno/zro2@sba-15 nanocatalysts for methanol synthesis from the catalytic hydrogenation of co2, Applied Catalysis B: Environmental 258 (2019) 117941. doi:10.1016/j.apcatb.2019.117941.

[19] J. Rouquerol, P. Llewellyn, F. Rouquerol, et al., Is the bet equation applicable to microporous adsorbents, Stud. Surf. Sci. Catal 160 (07) (2007) 49–56.

[20] O. Scholder, scholi/pyspm v0.2.20 (2019). doi:10.5281/ZENODO.2650457.
URL https://zenodo.org/record/2650457

[21] M. J. Frisch, G. W. Trucks, H. B. Schlegel, G. E. Scuseria, M. A. Robb, J. R. Cheeseman, G. Scalmani, V. Barone, G. A. Petersson, H. Nakatsuji, X. Li, M. Caricato, A. V. Marenich, J. Bloino, B. G. Janesko, R. Gomperts, B. Mennucci, H. P. Hratchian, J. V. Ortiz, A. F. Izmaylov, J. L. Sonnenberg, D. Williams-Young, F. Ding, F. Lipparini, F. Egidi, J. Goings, B. Peng, A. Petrone, T. Henderson, D. Ranasinghe, V. G. Zakrzewski, J. Gao, N. Rega, G. Zheng, W. Liang, M. Hada, M. Ehara, K. Toyota, R. Fukuda, J. Hasegawa, M. Ishida, T. Nakajima, Y. Honda, O. Kitao, H. Nakai, T. Vreven, K. Throssell, J. A. Montgomery, Jr., J. E. Peralta, F. Ogliaro, M. J. Bearpark, J. J. Heyd, E. N. Brothers, K. N. Kudin, V. N. Staroverov, T. A. Keith, R. Kobayashi, J. Normand, K. Raghavachari, A. P. Rendell, J. C. Burant, S. S. Iyengar, J. Tomasi, M. Cossi, J. M. Millam, M. Klene, C. Adamo, R. Cammi, J. W. Ochterski, R. L. Martin, K. Morokuma, O. Farkas, J. B. Foresman, D. J. Fox, Gaussian˜16 Revision C.01, gaussian Inc. Wallingford CT (2016).

[22] A. D. Becke, Density-functional thermochemistry. i. the effect of the exchange-only gradient correction, The Journal of Chemical Physics 96 (3) (1992) 2155–2160. arXiv:https://doi.org/10.1063/1.462066, doi:10.1063/1.462066.
URL https://doi.org/10.1063/1.462066

[23] C. Lee, W. Yang, R. G. Parr, Development of the colle-salvetti correlation-energy formula into a functional of the electron density, Physical Review B 37 (1988) 785–789. doi:10.1103/PhysRevB.37.785.
URL https://link.aps.org/doi/10.1103/PhysRevB.37.785

[24] P. J. Stephens, F. J. Devlin, C. F. Chabalowski, M. J. Frisch, Ab initio calculation of vibrational absorption and circular dichroism spectra using density functional force fields, The Journal of Physical Chemistry 98 (45) (1994) 11623–11627. arXiv:https://doi.org/10.1021/j100096a001, doi:10.1021/j100096a001.
URL https://doi.org/10.1021/j100096a001

[25] S. Grimme, S. Ehrlich, L. Goerigk, Effect of the damping function in dispersion corrected density functional theory, Journal of Computational Chemistry 32 (7) (2011) 1456–1465. arXiv:https://onlinelibrary.wiley.com/doi/pdf/10.1002/jcc.21759, doi:https://doi.org/10.1002/jcc.21759.
URL https://onlinelibrary.wiley.com/doi/abs/10.1002/jcc.21759

[26] Ł. Laskowski, M. Laskowska, M. Dulski, M. Zubko, J. Jelonkiewicz, M. Perzanowski, N. Vila, A. Walcarius, Multi-step functionalization procedure for fabrication of vertically aligned mesoporous silica thin films with metal-containing molecules localized at the pores bottom, Microporous and Mesoporous Materials 274 (2019) 356–362.

[27] M. Laskowska, I. Kityk, M. Dulski, J. Jedryka, A. Wojciechowski, J. Jelonkiewicz, M. Wojtyniak, Ł. Laskowski, Functionalized mesoporous silica thin films as a tunable nonlinear optical material, Nanoscale 9 (33) (2017) 12110–12123.

[28] D. Zhao, J. Feng, Q. Huo, N. Melosh, G. H. Fredrickson, B. F. Chmelka, G. D. Stucky, Triblock copolymer syntheses of mesoporous silica with periodic 50 to 300 angstrom pores, science 279 (5350) (1998) 548–552.

[29] D. Zhao, J. Sun, Q. Li, G. D. Stucky, Morphological control of highly ordered mesoporous silica sba-15, Chemistry of materials 12 (2) (2000) 275–279.

[30] Z. Wang, B. Chen, G. Quan, F. Li, Q. Wu, L. Dian, Y. Dong, G. Li, C. Wu, Increasing the oral bioavailability of poorly water-soluble car-

bamazepine using immediate-release pellets supported on sba-15 mesoporous silica, International journal of nanomedicine (2012) 5807–5818.

[31] P. Wei, G. Tian, H. Yu, Y. Qian, Synthesis of a novel organic-inorganic hybrid mesoporous silica and its flame retardancy application in pc/abs, Polymer degradation and stability 98 (5) (2013) 1022–1029.

[32] M. Laskowska, I. Kityk, O. Pastukh, M. Dulski, M. Zubko, J. Jedryka, K. Cpałka, P. M. Zieliński, Ł. Laskowski, Nanocomposite for photonics—nickel pyrophosphate nanocrystals synthesised in silica nanoreactors, Microporous and Mesoporous Materials 306 (2020) 110435.

[33] G. Mason, The effect of pore space connectivity on the hysteresis of capillary condensation in adsorption—desorption isotherms, Journal of Colloid and Interface Science 88 (1) (1982) 36–46.

[34] G. Dubois, R. J. Corriu, C. Reyé, S. Brandès, F. Denat, R. Guilard, First organic–inorganic hybrid materials with controlled porosity incorporating cyclam units, Chemical Communications (22) (1999) 2283–2284.

[35] M. Laskowska, Ł. Laskowski, K. Dzilinski, Mesoporous silica functionalized by nickel-cyclam molecules: preparation and resonance raman study, Current Topics in Biophysics 35 (1) (2012) 11–18.

[36] M. Campos-Vallette, S. Diez, R. Muñoz, et al., Specular reflectance infrared spectra of the macrocycles cyclam and cyclamdione and their cu (ii) complexes deposited onto a smooth copper surface, Vibrational Spectroscopy 15 (2) (1997) 201–209.

[37] H. Dodzitik, R. Kolinski, B. Koeybut-Daszkiewicz, Infrared spectra and structure of 1, 4, 8, 11-tetra-azacycotetradecanes, Spectrochimica Acta Part A: Molecular Spectroscopy 29 (3) (1973) 511–521.

[38] I. Vera-Estrada, J. Uribe-Godinez, O. Jimenez-Sandoval, Study of m (iii)-cyclam (m= rh, ru; cyclam= 1, 4, 8, 11-tetraazacyclotetradecane) complexes as novel methanol resistant electrocatalysts for the oxygen reduction reaction, RSC advances 10 (38) (2020) 22586–22594.

[39] K. Nakamoto, Infrared and Raman spectra of inorganic and coordination compounds, part B: applications in coordination, organometallic, and bioinorganic chemistry, John Wiley & Sons, New Jersey, 2009.

[40] K. R. Gorantla, B. S. Mallik, Computational mechanistic study on molecular catalysis of water oxidation by cyclam ligand-based iron complex, Theoretical Chemistry Accounts 139 (10) (2020) 161.

[41] M. Dulski, M. Laskowska, S. Sułowicz, T. Krzykawski, O. Pastukh, P. Zieliński, P. Pawlik, A. Nowak, et al., The impact of the functionalization of silica mesopores on the structural and biological features of sba-15, Microporous and Mesoporous Materials 306 (2020) 110453.

[42] B. Bosnich, M. Tobe, G. Webb, Complexes of nickel (ii) with a cyclic tetradentate secondary amine, Inorganic Chemistry 4 (8) (1965) 1109–1112.

[43] G. Diaz, E. Clavijo Campos, M. Campos Vallette, M. Saavedra, S. Diez, R. Munoz, Specular reflectance infrared spectra of the macrocycles cyclam and cyclamdione and their cu (ii) complexes deposited onto a smooth copper surface (1997).

[44] V. Pelmenschikov, Y. Guo, H. Wang, S. P. Cramer, D. A. Case, Fe–h/d stretching and bending modes in nuclear resonant vibrational, raman and infrared spectroscopies: Comparisons of density functional theory and experiment, Faraday discussions 148 (2011) 409–420.

[45] E. V. Basiuk, C. C. Ocampo-Bravo, V. Gómez-Vidales, M. Kakazey, V. A. Basiuk, Generation of paramagnetic centers in carboxylated materials via coordination attachment of diamagnetic tetraazamacrocyclic complexes of nickel (ii), Journal of Materials Science 55 (13) (2020) 5364–5377.

[46] V. Bykov, O. Koroleva, A. Osipov, Structure of silicate melts: Raman spectroscopic data and thermodynamic simulation results, Geochemistry International 47 (2009) 1067–1074.

[47] P. F. McMillan, G. H. Wolf, B. T. Poe, Vibrational spectroscopy of silicate liquids and glasses, Chemical Geology 96 (3-4) (1992) 351–366.

[48] D. Lin-Vien, N. B. Colthup, W. G. Fateley, J. G. Grasselli, The handbook of infrared and Raman characteristic frequencies of organic molecules, Elsevier, 1991.

[49] B. Parkinson, D. Holland, M. E. Smith, C. Larson, J. Doerr, M. Affatigato, S. A. Feller, A. Howes, C. Scales, Quantitative measurement of q3 species in silicate and borosilicate glasses using raman spectroscopy, Journal of Non-Crystalline Solids 354 (17) (2008) 1936–1942.

[50] D. Ginter, G. Went, A. Bell, C. Radke, A physicochemical study of the againg of colloidal silica gels used in zeolite y synthesis, Zeolites 12 (6) (1992) 733–741.

[51] P. K. Dutta, B. Del Barco, Raman spectroscopic studies of zeolite framework. hydrated zeolite a and the influence of cations, The Journal of Physical Chemistry 89 (10) (1985) 1861–1865.

[52] G. Socrates, Infrared and Raman characteristic group frequencies: tables and charts, John Wiley & Sons, 2004.

[53] J. Tan, S. Zhao, W. Wang, G. Davies, X. Mo, The effect of cooling rate on the structure of sodium silicate glass, Materials Science and Engineering: B 106 (3) (2004) 295–299.

[54] W. L. Konijnendijk, J. Stevels, The structure of borosilicate glasses studied by raman scattering, Journal of Non-Crystalline Solids 20 (2) (1976) 193–224.

[55] Y. Borodko, J. W. Ager, G. E. Marti, H. Song, K. Niesz, G. A. Somorjai, Structure sensitivity of vibrational spectra of mesoporous silica sba-15 and pt/sba-15, The Journal of Physical Chemistry B 109 (37) (2005) 17386–17390.

[56] D. W. Matson, S. K. Sharma, J. A. Philpotts, The structure of high-silica alkali-silicate glasses. a raman spectroscopic investigation, Journal of non-crystalline solids 58 (2-3) (1983) 323–352.

[57] P. Chaudhuri, K. Wieghardt, The chemistry of 1, 4, 7-triazacyclononane and related tridentate macrocyclic compounds, Progress in Macrocyclic Chemistry 35 (1987) 329–436.

[58] R. D. Bach, D. S. Shobe, H. B. Schlegel, C. J. Nagel, Thermochemistry of iron chlorides and their positive and negative ions, The Journal of Physical Chemistry 100 (21) (1996) 8770–8776.

[59] H. Kanno, J. Hiraishi, A raman study of aqueous solutions of ferric nitrate, ferrous chloride and ferric chloride in the glassy state, Journal of Raman Spectroscopy 12 (3) (1982) 224–227.

[60] L. Scholten, C. Schmidt, P. Lecumberri-Sanchez, M. Newville, A. Lanzirotti, M.-L. C. Sirbescu, M. Steele-MacInnis, Solubility and speciation of iron in hydrothermal fluids, Geochimica et Cosmochimica Acta 252 (2019) 126–143.

[61] P. Dillmann, F. Mazaudier, S. Hœrlé, Advances in understanding atmospheric corrosion of iron. i. rust characterisation of ancient ferrous artefacts exposed to indoor atmospheric corrosion, Corrosion science 46 (6) (2004) 1401–1429.

[62] S. Reguer, D. Neff, L. Bellot-Gurlet, P. Dillmann, Deterioration of iron archaeological artefacts: micro-raman investigation on cl-containing corrosion products, Journal of Raman Spectroscopy: An International Journal for Original Work in all Aspects of Raman Spectroscopy, Including Higher Order Processes, and also Brillouin and Rayleigh Scattering 38 (4) (2007) 389–397.

[63] S. Li, L. Hihara, A micro-raman spectroscopic study of marine atmospheric corrosion of carbon steel: the effect of akaganeite, Journal of the Electrochemical Society 162 (9) (2015) C495.

[64] D. Neff, L. Bellot-Gurlet, P. Dillmann, S. Reguer, L. Legrand, Raman imaging of ancient rust scales on archaeological iron artefacts for long-term atmospheric corrosion mechanisms study, Journal of Raman Spectroscopy: An International Journal for Original Work in all Aspects of Raman Spectroscopy, Including Higher Order Processes, and also Brillouin and Rayleigh Scattering 37 (10) (2006) 1228–1237.

[65] X. X. Han, R. S. Rodriguez, C. L. Haynes, Y. Ozaki, B. Zhao, Surface-enhanced raman spectroscopy, Nature Reviews Methods Primers 1 (1) (2021) 87.

[66] M. Skalska, M. Durak-Kozica, Experimental and analytical procedures for the tof-sims measurement data of membranous structures, Bio-Algorithms and Med-Systems 19 (1) (2023) 64–68.

doi:10.5604/01.3001.0054.1935.
URL http://dx.doi.org/10.5604/01.3001.0054.1935

[67] G. Estephane, C. Lancelot, P. Blanchard, V. Dufaud, S. Chambrey, N. Nuns, J. Toufaily, T. Hamiye, C. Lamonier, W-sba based materials as efficient catalysts for the ods of model and real feeds: Improvement of their lifetime through active phase encapsulation, Applied Catalysis A: General 571 (2019) 42–50. doi:https://doi.org/10.1016/j.apcata.2018.12.007.
URL https://www.sciencedirect.com/science/article/pii/S0926860X18305969

[68] I. Pethes, I. Bakó, L. Pusztai, Chloride ions as integral parts of hydrogen bonded networks in aqueous salt solutions: the appearance of solvent separated anion pairs, Phys. Chem. Chem. Phys. 22 (2020) 11038–11044. doi:10.1039/D0CP01806F.
URL http://dx.doi.org/10.1039/D0CP01806F

[69] W. J. Stevens, K. Lebeau, M. Mertens, G. Van Tendeloo, P. Cool, E. F. Vansant, Investigation of the morphology of the mesoporous sba-16 and sba-15 materials, The Journal of Physical Chemistry B 110 (18) (2006) 9183–9187.

[70] M. Etienne, A. Walcarius, Analytical investigation of the chemical reactivity and stability of aminopropyl-grafted silica in aqueous medium, Talanta 59 (6) (2003) 1173–1188.

[71] J. R. Jezorek, K. H. Faltynski, L. G. Blackburn, P. J. Henderson, H. D. Medina, Silica-bound complexing agents: some aspects of synthesis, stability and pore size, Talanta 32 (8) (1985) 763–770.

[72] M. Etienne, S. Goubert-Renaudin, Y. Rousselin, C. Marichal, F. Denat, B. Lebeau, A. Walcarius, Multiarm cyclam-grafted mesoporous silica: a strategy to improve the chemical stability of silica materials functionalized with amine ligands, Langmuir 25 (5) (2009) 3137–3145.

[73] S. Sayen, A. Walcarius, Electrochemical modulation of the ligand properties of organically modified mesoporous silicas, Journal of Electroanalytical Chemistry 581 (1) (2005) 70–78.

[74] A. Walcarius, M. Etienne, C. Delacote, Uptake of inorganic hgii by organically modified silicates: Influence of ph and chloride concentration

on the binding pathways and electrochemical monitoring of the processes, Analytica chimica acta 508 (1) (2004) 87–98.

[75] D. Gaffney, N. H. Abdallah, J. C. Cooney, F. R. Laffir, K. E. Cassimjee, P. Berglund, U. Hanefeld, E. Magner, Preparation and characterisation of a ni2+/co2+-cyclam modified mesoporous cellular foam for the specific immobilisation of his6-alanine racemase, Journal of Molecular Catalysis B: Enzymatic 109 (2014) 154–160.